ROYAL SOCIETY OF CHEMISTRY

PAPER

Check for updates

Drag reduction and antifouling of a spontaneous fast moving air film†

Defeng Yan, [ID] [ab] Junyi Lin,[a] Bingzhen Zhang,[a] Song Zhang,[a] Siying Ling*[c] and Jinlong Song [ID] *[ab]

Minimizing frictional resistance and preventing the attachment of marine organisms are extremely important for global ship navigation to reduce energy consumption and carbon emissions. However, there is still a lack of an effective and environmentally-friendly drag reduction and antifouling method. Here, we propose a spontaneous fast-moving air film to resolve this problem. We first developed a serial brachistochrone-shaped superhydrophobic pattern to easily capture underwater air bubbles and realize the spontaneous and directional transportation of bubbles with an average velocity of 444 mm s^{-1} that is the fastest in the whole world. Then, the continuous supply of air bubbles and serial brachistochrone-shaped superhydrophobic pattern were combined to form a spontaneous fast-moving air film, which not only prevents the escape of supplied air bubbles but also replenishes the air film on a superhydrophobic surface. The spontaneous fast-moving air film showed an amazing 27% drag reduction rate and simultaneous 80% antifouling rate, which was an outstanding capability that had never been reported before. This effective and environmentally-friendly drag reduction and antifouling method will minimize energy consumption and carbon emissions and has strong implications for global sustainable development.

1 Introduction

To protect the future of mankind, 178 countries signed the *Paris Agreement* with reduce the emission of carbon dioxide.[1,2] Ship navigation is a major energy consumer and carbon emitter, which consumed about 320 million tons of fuel and emitted more than 1 billion tons of CO_2 in 2022.[3] Reducing the drag of a ship is considered to be the most effective method to reduce its energy consumption and carbon emission.[4] The frictional resistance originating from the friction between the surface of a ship's hull and surrounding water is the major component of the ship's water resistance.[5,6] In addition, attached marine organisms originating from biofouling can further increase the frictional resistance of the ship.[7–9] Therefore, minimizing frictional resistance and preventing the attachment of marine organisms are of great significance.[10]

Constructing microstructures inspired by shark skin is a popular method to reduce the frictional resistance of a subaqueous object.[11] However, due to their lack of antifouling capability, marine organisms can easily attach to sharkskin-like microstructures, which in turn increases the frictional resistance.[12,13] Injecting air bubbles onto the ship's bottom is a more practical method of drag-reduction and has been applied in many large ships, such as ships carrying ore or liquefied natural gas. However, air bubbles are difficult to anchor to the ship's bottom, and there is a heavy escape rate, resulting in a low drag reduction rate.[14–16] In recent years, a superhydrophobic surface has been proposed to reduce frictional resistance because of its self-air film which is stored in surface microstructures.[17–20] However, this air film is easily broken and flows away, leaving a disappeared drag reduction phenomenon.[21–26] For marine antifouling, many chemical coatings are applied to kill the fouling organisms.[27,28] However, those coatings have poor antifouling capability and show great toxicity to marine organisms, endangering the marine environment.[29] Therefore, a more effective and environmentally-friendly drag reduction and antifouling method still needs to be explored.

In this work, we first optimally designed a serial cycloid-shaped pattern (SCP) which could spontaneously capture underwater air bubbles to realize the spontaneous and directional transportation of bubbles with an average velocity of 444 mm s^{-1}. Theoretical analysis was conducted to analyze the reason for the fast transportation of air bubbles. We then combined the continuous supply of air bubbles and SCP to form a spontaneous fast-moving air film, which not only prevents the escape of supplied air bubbles but also replenishes the air film on a superhydrophobic surface, showing an amazing 27% drag reduction rate and simultaneous 80% antifouling rate. This

[a]State Key Laboratory of High-performance Precision Manufacturing, Dalian University of Technology, Dalian Liaoning, 116024, China. E-mail: songjinlong@dlut.edu.cn

[b]Key Laboratory for Micro/Nano Technology and System of Liaoning Province, Dalian University of Technology, Dalian, Liaoning 116024, China

[c]College of Engineering, Shantou University, Shantou Guangdong, 515063, China. E-mail: syling@stu.edu.cn

† Electronic supplementary information (ESI) available. See DOI: https://doi.org/10.1039/d4ta03343d

effective and environmentally-friendly drag reduction and antifouling method will save a large amount of energy and promote the sustainable development of the whole world.

2 Experimental section

2.1 Materials

1060 aluminum sheets (Al, surface-free energy of 980 mJ m^{-2}) were purchased from Shenzhen Hongwang Co., Ltd (China). Anhydrous ethanol (surface-free energy of 22 mJ m^{-2}) was bought from Tianjin Kemio Chemical Reagent Co., Ltd (China). Fluoroalkylsilane [FAS, $C_8F_{13}H_4Si(OCH_2CH_3)_3$, containing a –$CF_3$ group with 6 mJ m^{-2} surface-free energy and a –CF_2 group with 18 mJ m^{-2} surface-free energy] was provided by Degussa Co. Ltd (Germany). Marine plants and clownfish were purchased from the local marine pet market. Seawater (surface-free energy of 72 mJ m^{-2}) was obtained from the Bohai Sea near Dalian.

2.2 Fabrication of samples

Preparation of serial brachistochrone-shaped pattern (SBP). A diagram of the preparation of the SBP is shown in **Figure S1**.† The Al sheet after cleaning was etched *via* a laser (SK-CX30, Shanghai Sanke Laser Technology Co. Ltd., China) to construct micro-rough structures. Next, the etched Al sheet was immersed in a 5 wt% FAS ethanol solution for 1.5 h. After drying, a superhydrophobic Al surface was obtained. Then, the exterior surrounding region of the superhydrophobic Al surface was processed again with the above laser to remove the FAS (**Figure S2**†). Finally, an SBP composed of an exterior surrounding a superhydrophilic region and interior superhydrophobic region was obtained.

Preparation of rectangular pattern (RP). The fabrication processes were similar to the above, but the pattern was rectangular.

Preparation of entire superhydrophobic surface. The Al sheet was etched by the aforementioned laser first, and then, a superhydrophobic Al surface was obtained by FAS modification.

2.3 Sample characterization

The microstructure of the surface was observed by a scanning electron microscope (SEM, JSM-6360LV, Japan). The corresponding elemental compositions were characterized by an energy dispersive spectroscope (EDS, JSM-6360LV, Japan). The water contact angle (WCA) in air and air contact angle (ACA) underwater were measured by a contact angle meter (DSA100, Krüss, Germany) using a water droplet of 4.1 μL and an air bubble of 3 μL at ambient temperature.

2.4 Underwater air bubble transportation

The equipment for an underwater air bubble transportation experiment was self-made to evaluate the transportation capability of the underwater air bubble on different samples (**Figure S3**†). The water depth of the underwater bubble transportation experiment was 30 mm. To ensure that the air bubbles were captured by the pattern, the bubble volume and distance between the bubble outlet and sample surface were 40 μL and 2 mm, respectively. All air bubble transportation experiments were pre-covered in an 80 μL air film. The release of air bubbles was controlled by a precision dispensing pump (LSP02-2A, Longer Pump). The underwater air bubble transportation behavior was recorded by a high-speed camera (1000 frames, DSC-RX10M3, Sony, Japan).

2.5 Underwater drag reduction

The underwater drag reduction experimental system was self-made to evaluate the drag reduction capability of the different samples. The sample platform could fix the different experiment samples, and one side of the sample platform was connected to a force sensor (DYX-306, Bengbu Sensing System Engineering Co. Ltd, China). The underwater free air bubbles which were generated by a supplier of continuous air bubbles (ES-3910, Anyuan Huaqun Technology Co. Ltd, China) on one side of the sample platform were captured by the SBP to form a constrained air film and were quickly transported to the other side of the SBP. The underwater drag reduction rate was the ratio of the underwater resistance of the common Al surface without bubble supply with the underwater resistance of the test sample with bubble supply subtracted, to the underwater resistance of the common Al surface without bubble supply, where the water flow rate was 0.5 m s^{-1}, and the air bubble flux was 0.4 L min^{-1}.

2.6 Marine antifouling

The marine antifouling test included an anti-diatom adhesion test and an antifouling test in a simulated marine environment.

For the anti-diatom adhesion test, we placed the common Al surface, superhydrophobic surface, SBP without bubble supply, and SBP with bubble supply in water containing diatoms and provided light for diatom growth. In the anti-diatom adhesion test, we recorded the images of the different samples every 2 days and calculated the corresponding diatom coverage rate which was the ratio of the area covered by diatoms to the test surface area. After 8 days, all the samples were taken out and observed with an optical microscope (MV-EM200C, Microvision Intelligent Manufacturing Technology Co. Ltd., China) to evaluate whether the sample surfaces were fouled by the diatoms.

For the antifouling test in the simulated marine environment, we placed the common Al surface, SBP without bubble supply, and SBP with bubble supply into seawater from the Bohai Sea near Dalian. To better simulate the marine environment, we also added marine plants and some clownfish to the seawater. After 4 days, all the samples were taken out and observed by SEM and the elemental compositions of these samples were characterized by EDS to evaluate their antifouling capability in the marine environment.

This journal is © The Royal Society of Chemistry 2024

J. Mater. Chem. A, 2024, **12**, 19268–19276 | **19269**

3 Results and discussion

3.1 Spontaneous high-speed transportation of a single air bubble

We proposed that a spontaneous fast-moving air film could realize underwater drag reduction and antifouling. Thus, the first problem to be solved here is how to obtain the spontaneous high-speed transportation of a single air bubble. Actually, there were several methods to realize the spontaneous transportation of an air bubble, such as using 3D structures,[30–33] slippery grooves,[34–37] rectangular patterns,[38–40] and wedge-shaped patterns.[41–44] However, the transportation distance and velocity for the air bubble on those surfaces were not long or fast enough. Nepenthes is a superstar in the field of bionic engineering.[45–47] Its lip shows a serial arch-shaped pattern which can spontaneously transport a liquid over a long distance with considerable velocity. Inspired by the Nepenthes lip and famous brachistochrone curve (**Figures 1(a)** and **S4**),[48] a serial brachistochrone-shaped pattern (SBP) with several single brachistochrone-shaped patterns connected end to end was proposed, where r, θ_1, and θ_2 were the rotating circle radius, angle by which the rotating circle rotated from its origin position to the starting position of a single pattern, and the angle by which the rotating circle rotated from its origin position to the end position of a single pattern, respectively. The SBP was composed of an exterior surrounding superhydrophilic region with a water contact angle of 0° and an interior super-hydrophobic region with a water contact angle of 164°. The superhydrophobicity resulted from the combined function of the micro-rough structures fabricated by the laser and FAS with a low surface energy.[49–51] After laser etching again to remove the FAS, the superhydrophobicity was successfully transformed into superhydrophilicity. Underwater, the exterior surrounding superhydrophilic region showed superaerophobicity with an air contact angle of 162°, while the interior superhydrophobic region showed superaerophilicity with an air contact angle of 0° (**Fig. 1(b) and (c)**). The underwater free air bubbles could be easily captured by the SBP to form a constrained air bubble and simultaneously be spontaneously and directionally transported along the SBP (**Fig. 1(d)**, S5 and Video S1†). To obtain the critical parameters for the fastest transportation velocity, we conducted the single-factor experiment first and later Box–Behnken design optimization. For the parameters r, θ_1, θ_2, and k, when three of them were fixed, all the average transportation velocities of the
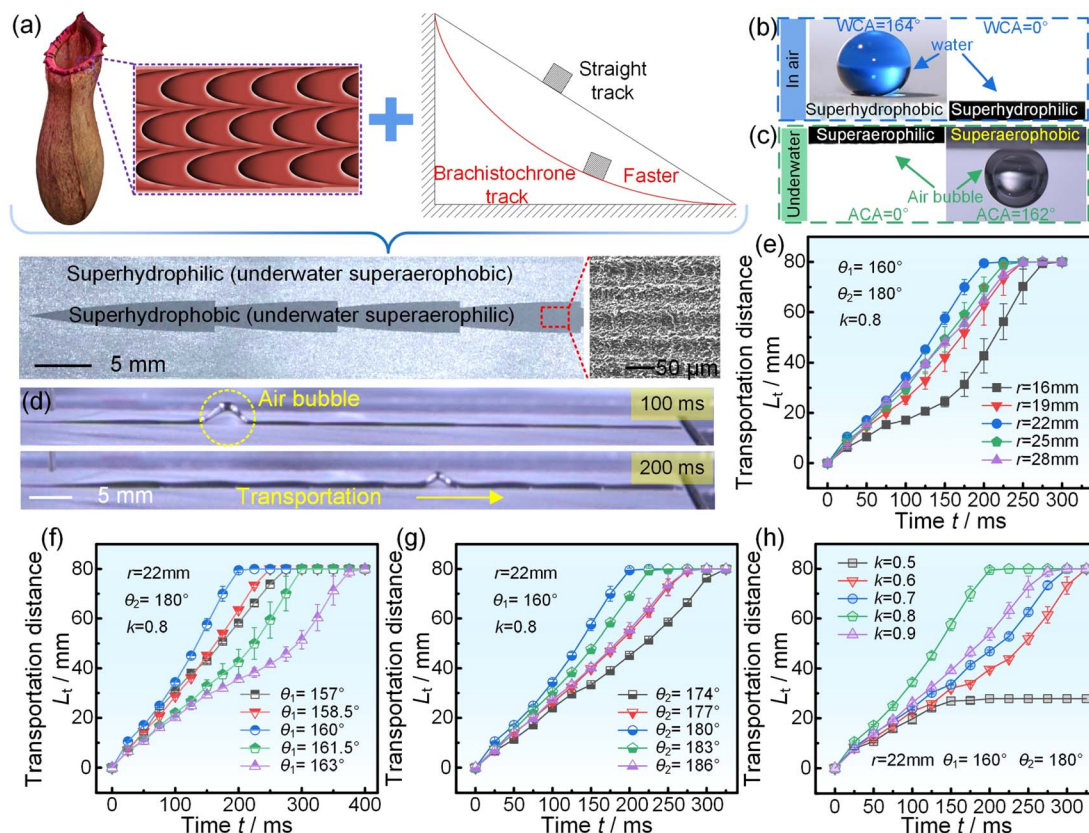

Fig. 1 Proposal for the SBP, wettability of the SBP in air and underwater, and variation of the transportation distance with the SBP parameters. (a) This SBP which is inspired by the Nepenthes lip and famous brachistochrone curve was proposed. (b) The wettability of a 4.1 μL water droplet on the SBP in air. (c) The wettability of a 3 μL air bubble on the SBP underwater. (d) The underwater transportation behavior of an air bubble on the SBP. (e) The variation of the underwater air bubble transportation distance with r, where the θ_1 of 160°, θ_2 of 180°, and k of 0.8 are fixed. (f) The variation of the underwater air bubble transportation distance with θ_1, where the r of 22 mm, θ_2 of 180°, and k of 0.8 are fixed. (g) The variation of the underwater air bubble transportation distance with θ_2, where the r of 22 mm, θ_1 of 160°, and k of 0.8 are fixed. (h) The variation of the underwater air bubble transportation distance with k, where the r of 22 mm, θ_1 of 160°, and θ_2 of 180° are fixed.

19270 | *J. Mater. Chem. A*, 2024, **12**, 19268–19276

This journal is © The Royal Society of Chemistry 2024

air bubble increased first and later decreased with an increase in the unfixed parameter (**Figures 1(e)–(h)**, **S6–S8**,† and †. A fast transportation velocity of the air bubble of 400 mm s^{-1} was obtained at r of 22 mm, θ_1 of 160°, θ_2 of 180°, and k of 0.8 in the single-factor experiment. Based on the aforementioned results, the SBP was further optimized by Box-Behnken design optimization. As shown in **Figure S9**, Tables S1–S3, and Video S3,† a faster transportation velocity of 415 mm s^{-1} was obtained at r of 22.1 mm, θ_1 of 160.4°, θ_2 of 180°, and k of 0.8.

We then studied the mechanism of influence of the SBP parameters (r, θ_1, θ_2, and k) on the transportation process of the air bubble. The force acting on the air bubble is shown in **Fig. 2(a)**. Once the air bubble comes into contact with the SBP, it will be subjected to the Laplace force F_L, capillary force F_C, water resistance force F_W, and pinning force F_P, which can be expressed as follows:

$$F = F_L + F_C - F_W - F_P \tag{1}$$

where F is the resultant force, F_L is the Laplace force, F_C is the capillary force, F_W is the resistance force from the water to the

transported air bubble, and F_P is the resistance force from the junction to the transported air bubble. For F_C, the F_C of the air bubble on the SBP can be ignored. For F_L, it is derived from the unbalanced Laplace pressure between the air bubble of the front and rear sides, which is the main driving force and can be given by:

$$F_L \sim \gamma l_f \cos \lambda_f - \gamma l_b \cos \lambda_b \tag{2}$$

where γ is the interfacial gas–water tension, l_f is the front contact line length of the air bubble, λ_f is the front ACA of the air bubble, l_b is the rear-side contact line length of the air bubble, λ_b is the rear-side ACA of the air bubble.[43] For the F_W, it can be described as:

$$F_W \sim \frac{1}{2} C\rho v(x)^2 S(x) \tag{3}$$

where C, ρ, $v(x)$, and $S(x)$ are the water drag coefficient, water density, instantaneous velocity of the air bubble at any transportation position x, and the cross-sectional area of the air
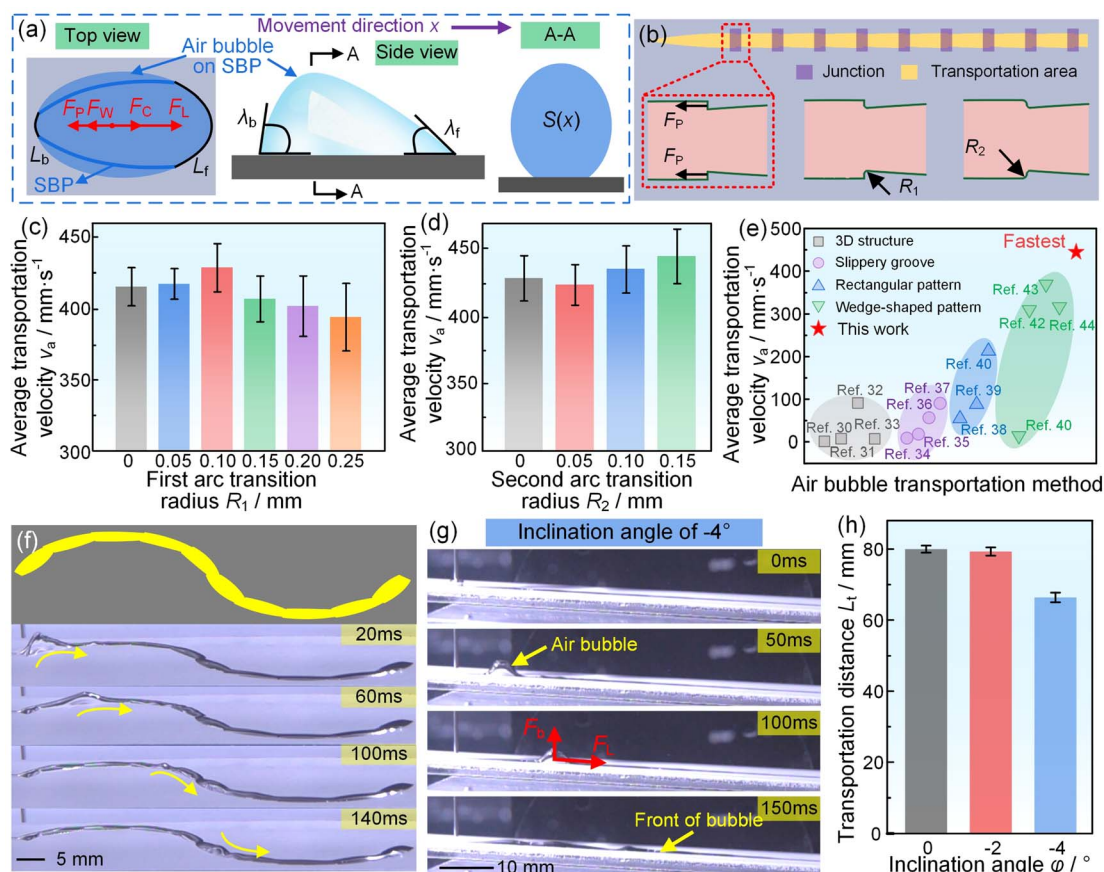

Fig. 2 Force analysis of the air bubble on the SBP, junction optimization of the SBP, and SBP can transport the bubble in various complex conditions. (a) Force analysis of the air bubble on the SBP. (b) Schematic of junction optimization. (c) Average transportation velocity of the air bubble on the SBP with different first arc transition radii. (d) Average transportation velocity of the air bubble on the SBP with different second arc transition radii, where the first arc transition radius is 0.1 mm. (e) Average transportation velocities for different air bubble transportation methods. The details of the air bubble transportation velocity are included in Table S4.† (f) The air bubble transportation process on a curved SBP track. (g) The air bubble transportation process on the SBP with an inclination angle of −4°. (h) The transportation distance of a 40 μL air bubble on the SBP with inclination angles of 0°, −2°, and −4°.

This journal is © The Royal Society of Chemistry 2024

J. Mater. Chem. A, 2024, **12**, 19268–19276 | **19271**

bubble at any transportation position x. F_P can be demonstrated as follows:

$$F_P \sim \gamma(w_w - w_n)(\cos \lambda_a - \cos \lambda_r) \qquad (4)$$

where w_w and w_n are the wide width and narrow width of the SBP, and λ_a, and λ_r are the advancing contact angle and receding contact angle of the air bubble at the junction. As shown in **Figure S6**,† decreasing r, increasing θ_1, decreasing θ_2, and increasing k led to an increase in the number of junctions, which meant that the air bubble was subjected to larger F_P, resulting in a decreasing average transportation velocity. Although increasing r, decreasing θ_1, and increasing θ_2 could decrease the junction number, they would increase the SBP area, meaning that the air bubble would be more spread out on the SBP with a larger area than that on the SBP with a smaller area, showing the decreasing difference of the Laplace pressure between the front and rear sides of the air bubble, decreasing F_L, and decreasing average transportation velocity (**Figure S10**†). In addition, according to eqn (4), decreasing k would increase F_P, resulting in decreasing average transportation velocity. If k was further decreased, the air bubble could not even achieve long-distance transportation (**Figure S8**†).

From the above force analysis, it can be seen that the air bubble was subjected to F_W and F_P, where F_W was difficult to decrease by optimal design. Therefore, we optimized the junction shape, using an arc to replace the wedge angle of the junction, which achieved decreasing F_P and increasing average transportation velocity (**Fig. 2(b)**). We first optimized the first arc transition radius R_1. The results showed that the average transportation velocity first increased and further decreased with increasing R_1, as shown in **Fig. 2(c)**. When R_1 was 0.1 mm, the average transportation velocity increased from 415 mm s^{-1} to 428 mm s^{-1} (Video S4†). We then optimized the second arc transition radius R_2, where R_1 was 0.1 mm. The results showed that when R_2 was 0.15 mm, the average transportation velocity was the fastest, reaching 444 mm s^{-1} (**Fig. 2(d)** and Video S4†). To confirm that our proposed SBP had faster transportation velocity than existing spontaneous air bubble transportation methods, we compared the SBP with these methods, as shown in **Figures 2(e)** and **S11**.[30–44] It was surprising that the transportation velocity of the air bubble on the SBP was almost 1.4–296 times as high as those on 3D structures, slippery grooves, rectangular patterns, or wedge-shaped patterns, which meant that the transportation velocity of the air bubble on the SBP was the fastest among the existing spontaneous air bubble transportation methods. Specifically, the details of the above spontaneous air bubble transportation methods are shown in Table S4†. In addition, besides a straight SBP, the air bubble could realize fast transportation on a curved SBP, as shown in **Fig. 2(f)** and Video S5†. Moreover, buoyancy had a significant influence on underwater bubble transportation: when $\varphi > 0°$, the buoyancy would promote air bubble transportation; when $\varphi < 0°$, the buoyancy would hinder air bubble transportation (**Figures S12** and **S13**†). It was amazing that the air bubble could even overcome the buoyancy and be spontaneously transported on the SBP with a transportation distance of 67 mm under a φ of −4°,

(**Fig. 2(g) and (h)**). The aforementioned results showed that our proposed SBP is not only the fastest in the spontaneous bubble transportation field but can also transport the bubble in various complex conditions.

3.2 Underwater drag reduction

We then confirmed the importance of spontaneous high-speed transportation of air bubbles on improving the drag reduction rate. We designed an underwater drag reduction experiment system which included a supplier of continuous air bubbles and samples with different patterns (**Fig. 3(a)**). Every sample with 40 mm width and 200 mm length had 9 rectangular patterns (RPs) or 9 SBPs. For the common Al surface, we found that the supplied underwater free air bubbles were not captured by the surface and touched the surface only under the influence of buoyancy, but eventually escaped mostly without any spontaneous moving air film, which resulted in a low bubble capture rate of less than 5% (**Fig. 3(b), (c)** and Video S6†). For the sample with RPs, some underwater free air bubbles were captured by the RP to form constrained air bubbles and a spontaneous moving air film (**Fig. 3(d)**). Although the constrained air bubbles on the RP could harvest some surrounding air bubbles, it is hard for them to catch up and harvest the air bubbles in front of them, still leaving some escaping bubbles with a bubble capture rate of 74%. For the sample with SBPs, many underwater free air bubbles were captured by the SBP to form constrained air bubbles which were bigger and moved faster than those on the RP and not only harvested the surrounding air bubbles but also caught up and harvested the air bubbles in front of them with a bubble capture rate of 95%, leaving a spontaneous fast-moving air film (**Fig. 3(e)**). Therefore, compared with RP, the constrained air bubbles on the SBP moved faster and captured more air bubbles (**Fig. 3(f)**). In addition, a bigger bubble provided a greater contact area to capture the underwater free air bubbles (**Fig. 3(g)**). Eventually, a virtuous cycle of fast movement-capture more bubbles-get bigger-fast movement was created on the SBP to guarantee a spontaneous fast-moving air film. We next recorded the underwater resistance force curves of the common Al surface, common Al surface with bubble supply, 9 RPs with bubble supply, and 9 SBPs with bubble supply and calculated their drag reduction rates compared with the common Al surface using MATLAB software, as shown in **Fig. 3(h)**, S14, and S15. The drag reduction rates for the common Al surface with bubble supply, 9 RPs with bubble supply, and 9 SBPs with bubble supply were 4.5%, 12.7%, and 17.5%, respectively. The higher drag reduction rate for the 9 SBPs with bubble supply resulted from the spontaneous fast-moving air film, which offered a heterogeneous slip boundary to reduce the drag experienced by water flowing on it.[52] Moreover, increasing the number of SBPs can increase the coverage of spontaneous fast-moving air film over the whole substrate surface. Under the condition of maintaining the presence of a spontaneous fast-moving air film, the maximum number of SBPs for the sample with 40 mm width and 200 mm length was 13, and the corresponding maximum drag reduction rate was as high as 27% (**Figure S16**†).
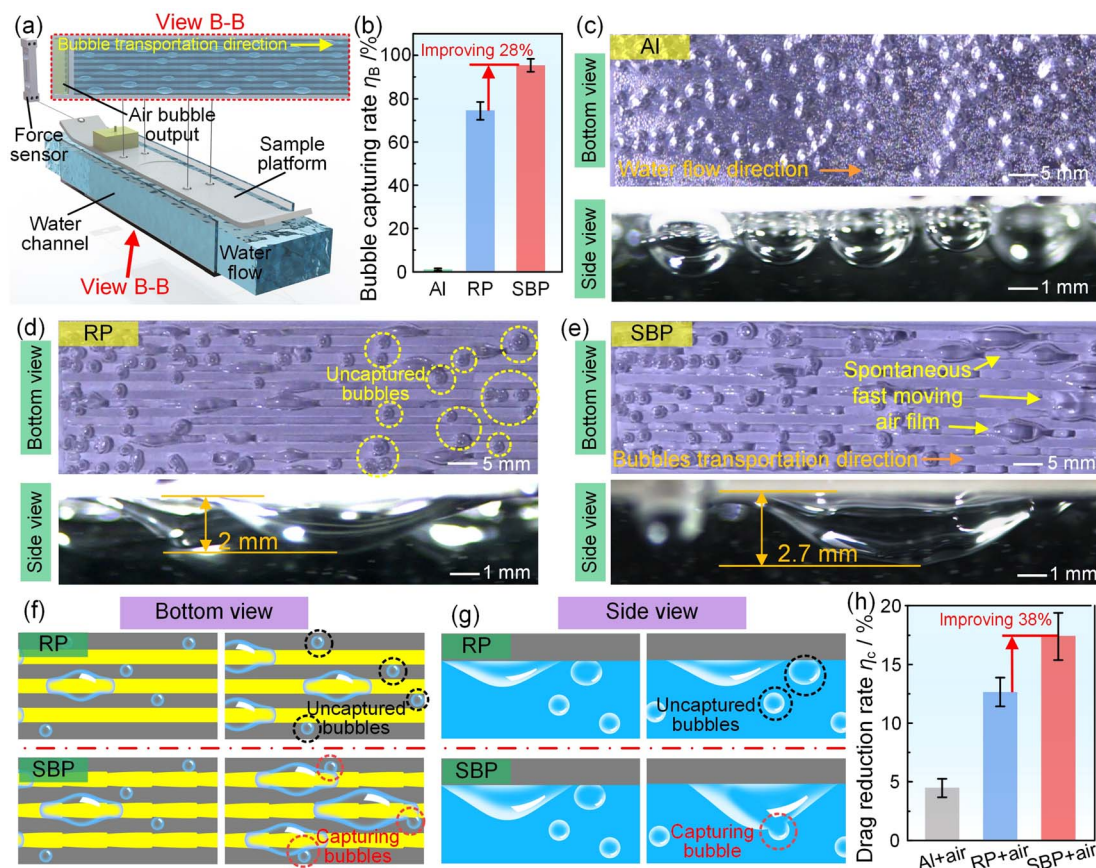
19272 | *J. Mater. Chem. A*, 2024, **12**, 19268–19276

This journal is © The Royal Society of Chemistry 2024

Fig. 3 The SBP has superb underwater drag reduction capability. (a) Schematic of the underwater drag reduction experimental system. (b) Bubble capture rate of the common Al surface, RP, and SBP. (c) Images of the bubbles on the common Al surface with a bottom view and a side view. (d) Images of the bubbles on the RP with a bottom view and a side view. (e) Images of the bubbles on the SBP with a bottom view and a side view. (f) Schematic of bubbles on the RP and SBP with a bottom view. (g) Schematic of bubbles on the RP and SBP with a side view. (h) Drag reduction rate of the common Al surface with bubble supply, RP with bubble supply, and SBP with bubble supply. The water flow rate and air bubble flux were 0.5 m s^{-1} and 0.4 L min^{-1}, respectively.

3.3 Marine antifouling

The marine fouling of the surface of a ship's hull first needs primary colonizers, such as diatoms or bacteria, to adhere on the surface, and then, other marine organisms use these primary colonizers as food to grow and breed. If the spontaneous fast-moving air film can prevent the attachment of primary colonizers, antifouling is expected to be realized. We first conducted an anti-diatom adhesion test using the experimental system shown in **Fig. 4(a)**. We placed four samples, the common Al surface, superhydrophobic Al surface, the SBP without bubble supply, and the SBP with bubble supply in water containing diatoms. After 8 days of immersion, the common Al surface was thickly covered with many diatoms (**Fig. 4(b), (b1)**), and the superhydrophobic surface and SBP without bubble supply were thinly covered with some diatoms. However, the SBP with bubble supply remained clean without any diatom coverage (**Fig. 4(b2)**). In addition, we calculated the diatom coverage rate with immersion time for the different samples. The diatom coverage rate for the common Al surface, superhydrophobic Al surface, and SBP without bubble supply grew very fast and exceeded 90% for 4 immersion days and exceeded

97% for 8 immersion days (**Fig. 4(c)**). However, the diatom coverage rate for the SBP with bubble supply after 8 immersion days was almost 0, showing a superb anti-diatom adhesion capability. To further investigate the marine antifouling capability of the SBP with bubble supply, we then conducted an antifouling test in the simulated marine environment, including seawater, sea fish, and marine plants, as shown in **Fig. 4(d)**. After 4 days of immersion, the whole common Al surface was corroded by the seawater and contaminated by the marine organisms (**Fig. 4(e)** and **S17†**). The SBP without bubble supply was also contaminated by the marine organisms. Chemical analysis indicated that the contaminant could be corrosion products, microorganisms, marine plant debris, and fish faeces (**Figures S18** and **S19†**). However, the macroscopic and microscopic morphology of the SBP with bubble supply remained unchanged, indicating that the primary colonizers in the seawater could not adhere to the surface, indirectly preventing the adhesion of other marine organisms. It is worth noting that the exterior surrounding region of the SBP with bubble supply is still easily fouled. Similarly, to maintain the presence of a spontaneous fast-moving air film, for the sample
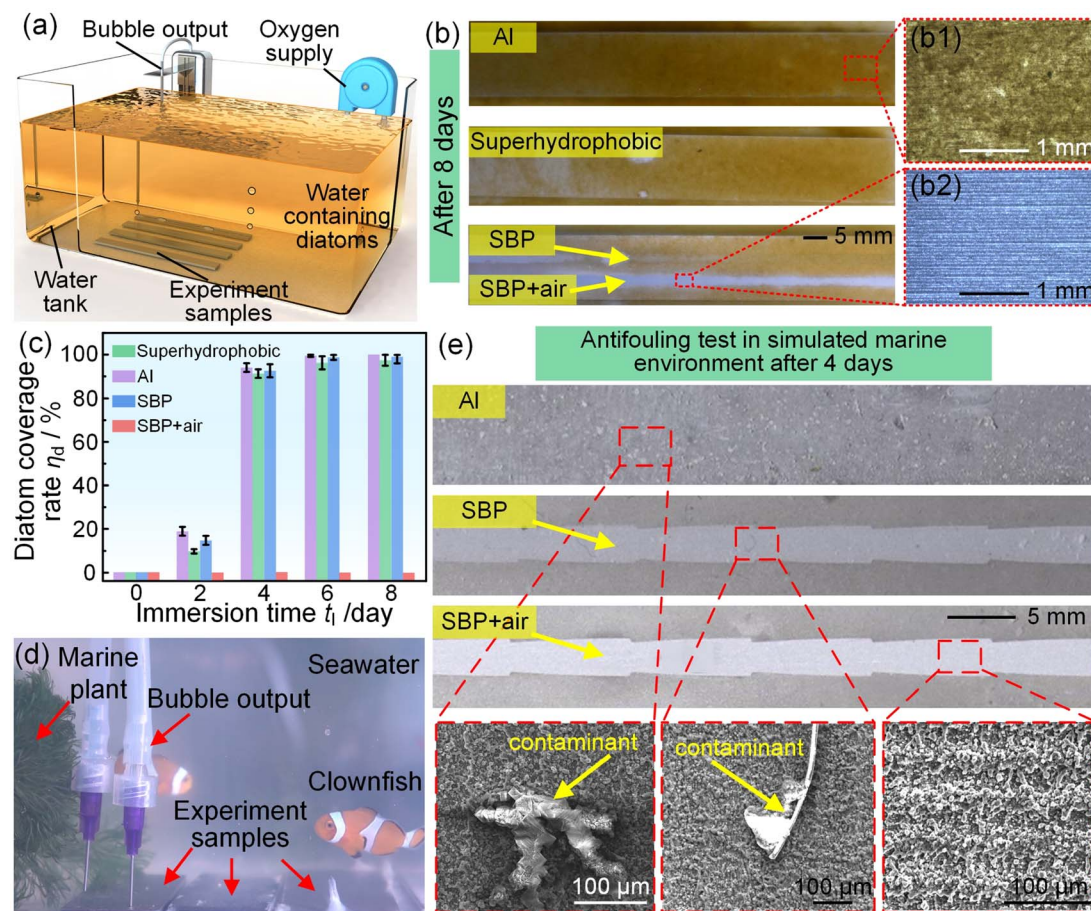
This journal is © The Royal Society of Chemistry 2024

J. Mater. Chem. A, 2024, **12**, 19268–19276 | **19273**

Fig. 4 The SBP has excellent marine antifouling capability. (a) Schematic of an anti-diatom adhesion test device. (b) Images of the different samples after the anti-diatom adhesion test for 8 days. (b1) Enlarged view of the common Al surface. (b2) Enlarged view of the SBP with bubble supply. (c) Diatom coverage rate for the common Al surface, superhydrophobic surface, SBP without bubble supply, and SBP with bubble supply at different immersion times. (d) Image of the antifouling test in the simulated marine environment. (e) Images and SEM images of the common Al surface, SBP without bubble supply, and SBP with bubble supply after the antifouling test for 4 days. The air bubble flux for the SBP when the air supply was 0.4 L min^{-1}.

with 40 mm width and 200 mm length, the maximum number of SBPs was 13, and the corresponding maximum marine antifouling rate was as high as 80% (**Figure S16†**).

4   Conclusions

In conclusion, a spontaneous fast-moving air film, which originated from the spontaneous and directional transportation of underwater air bubbles on a serial brachistochrone-shaped pattern (SBP), was proposed for drag reduction and antifouling. We first investigated the variation of the underwater air bubble transportation processes with the SBP parameters. The experimental results and theoretical analysis showed that the decreasing rolling circle radius r, increasing start rotation angle θ_1, decreasing end rotation angle θ_2, and increasing ratio of the narrow width to the wide width k led to an increase in the junction number. In addition, the increasing r, decreasing θ_1, and increasing θ_2 resulted in an increased SBP area. However, the increasing number of junctions and increasing SBP area would result in a decreased transportation velocity. Moreover,

the decreasing k even meant that the air bubble could not be transported over a long distance. We then obtained the fastest transportation velocity of 444 mm s^{-1} after the Box–Behnken design optimization and junction optimization strategy, which was faster than the existing underwater spontaneous bubble transportation method. Since the air bubble could be quickly transported on the SBP, the supplied underwater air bubbles could form a spontaneous fast-moving air film, which offered a heterogeneous slip boundary to reduce the drag experienced by water flowing on it. In addition, the spontaneous fast-moving air film could prevent the attachment of primary colonizers and achieve antifouling. Eventually, under the condition of maintaining the presence of a spontaneous fast-moving air film, we simultaneously achieved 27% underwater drag reduction and 80% marine antifouling by setting a suitable number of SBPs. This finding could maximize energy saving for ships and facilitate sustainable development for humans.

Data availability

The data that supports the findings of this study are available in the ESI† of this article.

Author contributions

Conflicts of interest

There are no conflicts to declare.

Acknowledgements

References

1 A. Goldthau and S. Tagliapietra, *Nature*, 2022, **612**, 627–630.
2 Z. Sun, Y. Liao, S. Zhao, X. Zhang, Q. Liu and X. Shi, *J. Mater. Chem. A*, 2022, **10**, 5174–5211.
3 X. Wang, Z. Li, X. Luo, S. Chang, H. Zhu, X. Guan and S. Wang, *MRS Energy Sustain.*, 2023, **10**, 247–260.
4 K. W. Yanuar, S. Pratama, B. Candra and B. Rahmat, *J. Mar. Sci. Appl.*, 2018, **17**, 165–172.
5 T. Wu, W. Chen, A. Zhao, P. He and H. Chen, *Ocean Eng.*, 2020, **218**, 107902.
6 S. Amini, S. Kolle, L. Petrone, O. Ahanotu, S. Sunny, C. Sutanto, S. Hoon, L. Cohen, J. Weaver, J. Aizenberg, N. Vogel and A. Miserez, *Science*, 2017, **357**, 668.
7 J. Tan, J. Xu, D. Wang, J. Yang and S. Zhou, *J. Mater. Chem. A*, 2020, **8**, 24086–24097.
8 W. Zhao, J. Yang, H. Guo, T. Xu, Q. Li, C. Wen, X. Sui, C. Lin, J. Zhang and L. Zhang, *Chem. Eng. Sci.*, 2019, **207**, 790–798.
9 H. Jin, L. Tian, W. Bing, J. Zhao and L. Ren, *Prog. Mater. Sci.*, 2022, **124**, 1008898.
10 I. Vakarelski, E. Klaseboer, A. Jetly, M. Mansoor, A. Aguirre-Pablo, D. Chan and S. Thoroddsen, *Sci. Adv.*, 2017, **3**, e1701558.
11 K. Choi, *Nature*, 2006, **440**, 754.
12 W. Jo, H. Kang, J. Choi, J. Jung, J. Hyun, J. Kwon, I. Kim, H. Lee and H. Kim, *Nano Lett.*, 2021, **21**, 5500–5507.
13 G. Bixler and B. Bhushan, *Adv. Funct. Mater.*, 2013, **23**, 4507–4528.
14 S. Wu, C. Hsu and T. Lin, *Ocean Eng.*, 2007, 83–93.
15 S. Ceccio, *Annu. Rev. Fluid. Mech.*, 2010, **42**, 183–203.
16 I. Kumagai, Y. Takahashi and Y. Murai, *Ocean Eng.*, 2015, **95**, 183–194.
17 D. Saranadhi, D. Chen, J. Kleingartner, S. Srinivasan, R. Cohen and G. McKinley, *Sci. Adv.*, 2016, **2**, e1600686.
18 I. Vakarelski, N. Patankar, J. Marston, D. Chan and S. Thoroddsen, *Nature*, 2012, **489**, 274–277.
19 U. Gunatilake, Y. Alvarez-Brana, E. Ojeda, L. Basabe-Desmonts and F. Benito-Lopez, *J. Mater. Chem. A*, 2022, **10**, 12832–12841.
20 X. Bai, X. Gou, J. Zhang, J. Liang, L. Yang, S. Wang, X. Hou and F. Chen, *Small*, 2023, **19**, 2206463.
21 C. Lee and C. Kim, *Phys. Rev. Lett.*, 2011, **106**, 14502.
22 J. Wei, J. Zhang, X. Cao, J. Huo, X. Huang and J. Zhang, *Nat. Commun.*, 2023, **14**, 2862.
23 H. Hu, J. Wen, L. Bao, L. Jia, D. Song, B. Song, G. Pan, M. Scaraggi, D. Dini, Q. Xue and F. Zhou, *Sci. Adv.*, 2017, **3**, e1603288.
24 W. Barthlott, T. Schimmel, S. Wiersch, K. Koch, M. Brede, M. Barczewski, S. Walheim, A. Wei, A. Kaltenmaier, A. Leder and H. Bohn, *Adv. Mater.*, 2010, **22**, 2325–2328.
25 L. Wang, D. Li, G. Jiang, X. Hu, R. Peng, Z. Song, H. Zhang, P. Fan and M. Zhong, *ACS Nano*, 2024, **18**, 12489–12502.
26 J. Busch, W. Barthlott, M. Brede, W. Terlau and M. Mail, *Philos. Trans. R. Soc. London, A*, 2019, **377**, 20180263.
27 O. Ferreira, P. Rijo, J. Gomes, R. Santos, S. Monteiro, c. Vilas-Boas, M. Correia, s. Almada, L. Alves, J. Bordado and E. Silva, *ACS Sustainable Chem. Eng.*, 2020, **8**, 12–17.
28 J. Choi, S. Lee, K. Ohkawa and D. Hwang, *ACS Nano*, 2021, 18566–18579.
29 I. Banerjee, R. Pangule and R. Kane, *Adv. Mater.*, 2011, **23**, 690–718.
30 Y. Wang, L. Zhang, W. Du, X. Zhou, Y. Guo, S. Zhao, D. Zhang and H. Chen, *Adv. Funct. Mater.*, 2023, **33**, 85–89.
31 X. Xue, C. Yu, J. Wang and L. Jiang, *ACS Nano*, 2016, **10**, 10887–10893.
32 X. Gao, F. Zhang, Z. Zhang, Z. Wang, Y. Song, G. Cheng and J. Ding, *ACS Appl. Mater. Interfaces*, 2023, **15**, 54119–54128.
33 C. Yu, M. Cao, Z. Dong, K. Li, C. Yu, J. Wang and L. Jiang, *Adv. Funct. Mater.*, 2016, **26**, 6830–6835.
34 X. Wang, H. Bai, J. Yang, Z. Li, Y. Wu, C. Yu, L. Jiang and M. Cao, *Small*, 2021, 17 2007803.
35 X. Wang, H. Bai, Z. Li, Y. Tian, T. Zhao and M. Cao, *Mater. Horiz.*, 2023, **10**, 3351–3359.
36 C. Yu, X. Zhu, K. Li, M. Cao and L. Jiang, *Adv. Funct. Mater.*, 2017, **27**, 1701605.
37 K. Zhuang, X. Yang, W. Huang, Q. Dai and X. Wang, *ACS Appl. Mater. Interfaces*, 2021, **13**, 61780–61788.
38 Z. Wang, J. Xiong, Y. Liao, M. Xie, D. Yang, C. Zhang, Y. Chen and Z. Zou, *Chem. Eng. J.*, 2023, **474**, 145352.
39 J. Yong, Q. Yang, J. Huo, X. Hou and F. Chen, *Int. J. Extrem. Manuf.*, 2022, **4**, 15002.
40 D. Xie, Y. Sun, Y. Wu, K. Wang, G. Wang, F. Zang and G. Ding, *Adv. Mater.*, 2023, **35**, e2208645.
41 X. Xiao, S. Li, X. Zhu, C. Zhang, F. Jiang, C. Yu and L. Jiang, *Nano Lett.*, 2021, **21**, 2117–2123.

This journal is © The Royal Society of Chemistry 2024

J. Mater. Chem. A, 2024, **12**, 19268–19276 | **19275**

42 Z. Liu, H. Zhang, Y. Han, L. Huang, Y. Chen, J. Liu, X. Wang, X. Liu and S. Ling, *ACS Appl. Mater. Interfaces*, 2019, **11**, 23808–23814.

43 H. Ma, M. Cao, C. Zhang, Z. Bei, K. Li, C. Yu and L. Jiang, *Adv. Funct. Mater.*, 2018, **28**, 1705091.

44 J. Song, Z. Liu, X. Wang, H. Liu, Y. Lu, X. Deng, C. J. Carmalt and I. P. Parkin, *J. Mater. Chem. A*, 2019, **7**, 13567–13576.

45 H. Chen, T. Ran, Y. Gan, J. Zhou, Y. Zhang, L. Zhang, D. Zhang and L. Jiang, *Nat. Mater.*, 2018, **17**, 935–942.

46 J. Zhang, A. Wang and S. Seeger, *Adv. Funct. Mater.*, 2013, **24**, 1074–1080.

47 H. Chen, P. Zhang, L. Zhang, H. L. Iu, Y. Jiang, D. Zhang, Z. Han and L. Jiang, *Nature*, 2016, **532**, 85–89.

48 E. Rodgers, *Am. J. Phys.*, 1946, **14**, 249–252.

49 D. Yan, Y. Chen, J. Liu and J. Song, *Small*, 2023, **19**, 2301745.

50 Y. Wang, Y. Sun, Y. Sun, X. Sui, B. Yuan, Y. Wang and W. Liang, *Prog. Org. Coat.*, 2024, **188**, 108167.

51 D. Yan, Y. Lu, J. Liu, Y. Chen, J. Sun and J. Song, *Nanoscale*, 2023, **15**, 11473–11481.

52 R. A. Verschoof, R. C. A. van der Veen, C. Sun and D. Lohse, *Phys. Rev. Lett.*, 2016, **117**, 104502.

19276 | *J. Mater. Chem. A*, 2024, **12**, 19268–19276

This journal is © The Royal Society of Chemistry 2024